



Vibrational Spectroscopies, Global Reactivity, Molecular Docking, Thermodynamic Properties and Linear and Nonlinear Optical Parameters of Monohydrate Arsenate Salt of 4-Aminopyridine

Noureddine Mhadhbi¹ · Souad Dgachi¹ · Ali Ben Ahmed² · Noureddine Issaoui³ · Samia Nasr⁴ · Riadh Badraoui⁵ · Bechir Badraoui⁶ · Houcine Naili¹

Received: 14 November 2022 / Accepted: 7 February 2023 / Published online: 14 February 2023
© The Tunisian Chemical Society and Springer Nature Switzerland AG 2023

Abstract

In this work, a structural and electronic properties of a novel organic arsenate template by 4-aminopyridine, with the general formula $(C_5H_7N_2)(C_5H_8N_2)[AsO_4] \cdot H_2O$ ((4-APH)(4-APH₂)[AsO₄]·H₂O) have been presented. The density functional theory (DFT) along with B3LYP hybrid functional is employed. The optimized structure was found to be in well consistent with the X-ray diffraction geometry. The examination of the vibrational spectrum was correlated by DFT calculation using the unit cell parameters obtained from the experiment data. Besides, the thermodynamic functions (heat capacity, entropy, enthalpy) from spectroscopic data by statistical methods were obtained for the range of temperature 100–1000 K. In addition, the molecular orbital calculations such as Natural Bond Orbitals (NBOs), AIM approach, HOMO–LUMO energy gap, NLO characteristic and Hirshfeld surface analysis were also performed with the same level of DFT. Electronic stability of the compound arising from hyper conjugative interactions and charge delocalization were also investigated based on the natural bond orbital (NBO) analysis. Molecular docking studies were also conducted as part of this study. The theoretical results showed an excellent agreement with the experimental values.

Keywords DFT approach · Frontier molecular orbital · Nonlinear optical parameters · Thermodynamic functions · Pharmacokinetics · Druggability

✉ Ali Ben Ahmed
ali.benahmed@isbs.usf.tn

- ¹ Laboratory of Solid State, Department of Chemistry, Faculty of Sciences of Sfax, University of Sfax, B.P. N°1171, 3000 Sfax, Tunisia
- ² Laboratory of Applied Physics, Department of Physics, Faculty of Sciences of Sfax, University of Sfax, B.P. N°802, 3018 Sfax, Tunisia
- ³ Laboratory of Quantum and Statistical Physics, Department of Physics, Faculty of Sciences of Monastir, University of Monastir, 5079 Monastir, Tunisia
- ⁴ Preparatory Institute for Engineering Studies Kairouan, Electrochemistry, Materials and Environment, University of Kairouan, Kairouan, Tunisia
- ⁵ Section of Histology-Cytology, Medicine Faculty of Tunis, University of Tunis El Manar, La Rabta, 1007 Tunis, Tunisia
- ⁶ Research Unity of Materials and Et Organic Synthesis, Preparatory Institute for Engineering Studies of Monastir, University of Monastir, 5019 Monastir, Tunisia

1 Introduction

Organic–inorganic hybrid compounds have attracted much attention in recent research due not only to their fascinating architectures, but also to their structural diversity and their excellent magnetic, luminescence, nonlinear optical (NLO), catalytic and electrical proprieties [1–6]. These properties emanate from their diverse structures that can be well predicted and designed under the guidance of coordination chemistry and crystal engineering [7–9]. Such materials have recently been the interest of many studies due to their attractive potential for application as insulators in the electronics industry. Among these hybrid compounds, organic salts of arsenate are particularly significant and their anions are interconnected by strong hydrogen bonds so as to build infinite networks with various geometries such as ribbons, chains or layers [10–12]. To benefit from these materials, a good knowledge of their structural characteristics is fundamental, not only for the design of other hybrid

compounds, but also for the prediction of their physico-chemical properties.

The compound $(C_5H_7N_2)(C_5H_8N_2)[AsO_4]\cdot H_2O$ was prepared in our laboratory [13]. Whereas its crystal structure has been previously reported, its physical and biological properties based on its crystal structure will be discussed in greater detail. The organic salts of arsenate contain mono and diprotonated 4-aminopyridine cations, an arsenate trianion and one water compound. The diprotonated 4-ammoniopyridinium dication $[C_5H_8N_2]^{2+}$ is disordered over two positions with refined site occupancies of 0.73 and 0.27 however the monoprotated 4-aminopyridinium cation $[C_5H_7N_2]^+$ is ordered. In the crystal, the As^{III} atom is coordinated by four O atoms in a slightly distorted tetrahedral geometry.

In addition, the quantum chemical methods are widely used for the investigation of theoretical modeling of drug functional materials; these methods provide powerful tools for studying molecular geometry, vibrational and molecular properties via Becke's three-parameter hybrid functional (B3LYP) and Density Functional Theory (DFT) [14, 15]. Therefore, in the present article it is planned to calculate the optimized molecular geometry and the vibrational spectra of this compound completely and to identify the various normal modes with wave number accuracy. Experimentally observed spectral data (FT-TR and FT-Raman) of the title compound were compared with the spectral data obtained by DFT/B3LYP method.

The molecular properties like dipole moment, polarizability, first static hyperpolarizability, NLO properties and molecular electrostatic potential surface, contour map have been calculated to get a better understanding of the properties of the title compound. Natural bond orbital (NBO) analysis has been applied to study the stability of the compound arising from charge delocalization. Various local and global reactivity descriptors along with thermo dynamical properties were theoretically calculated and described to reveal the characteristics of title compound. Furthermore, the comparison of chemical reactivity and biological activity has been done by calculating global and local reactivity parameters and performing molecular docking studies.

2 Chemicals and Materials

2.1 Synthesis

The single crystals of $(C_5H_7N_2)(C_5H_8N_2)[AsO_4]\cdot H_2O$ compound crystals were grown by slow evaporation, at room temperature. Details of the growth procedure and single crystal X-ray diffraction study were described elsewhere [13]. All materials used in this work were of reagent grade purity and were used as commercially obtained:

4-aminopyridine ($C_5H_6N_2$) (98%, SIGMA ALDRICH) and arsenic Acid (H_3AsO_4) (90.5%, SIGMA ALDRICH). Alcohol was used in this synthesis.

2.2 Spectroscopic Measurements

Raman spectrum was performed at room temperature using a LABRAM-Jobin Yvon set up. The excitation line was 630 nm from a Neon laser from 400 to 4000 cm^{-1} . The incident laser power was limited to 5 mW to avoid sample heating degradation. The laser beam was focused on to the sample through a $\times 50$ microscope objective. The IR spectrum was recorded from 400 to 4000 cm^{-1} on a BRUKER spectrometer with a spectral resolution of 2 cm^{-1} .

3 Computational Details

The DFT method using the Gaussian 09 software program [16] was used to perform molecular geometry optimization and vibrational wave number calculations. The DFT approach and effective core potentials (ECPs) (LANL2DZ basis and ECP built-in) have been utilized in order to represent the metal. The B3LYP method with 6–311++ G(d,p) basis set was used for all atoms except for the arsenic and nitrogen atoms. The geometry optimizations and frequency calculations of $(4-APH)(4-APH_2)[AsO_4]\cdot H_2O$ were carried out using the Becke's three-parameter hybrid exchange functional (B3) [17] combined with the Lee–Yang–Parr correlation functional (LYP) [18] in conjunction with the LanL2DZ basis set [19]. Geometric parameters from the theoretical structure were compared with the experimental X-ray diffraction data. The calculated vibrational wavenumbers were assigned using GaussView05 program [20] employed to generate visual presentations and verify the normal mode assignments. Various non-linear optical properties of the title compound such as dipole moment (μ), polarizability (α) and first static hyperpolarizability (β) values were also computed on theoretical computations. The electronic properties such as (HOMO) and (LUMO) energies were determined. The Natural Bond Orbital (NBO) [21] was calculated at B3LYP level using the basis set 6–311++ G(d,p). This analysis was done to give clear evidence of stabilization originating from hyper conjugation of various intramolecular interactions [22–25]. To get insight on the intermolecular H-bonding, the most important AIM topological parameters at bond critical points (BCP) of O–H and O...H contacts have been calculated by using the Multiwfn software [26]. The Molecular Electrostatic Potential (MEP) was also calculated using Gauss View. Additionally, the thermodynamic properties of the title compound were calculated at different temperatures, revealing the correlation between heat capacity (C), enthalpy (H) and entropy (S) with temperatures. The

Crystal Explorer 3.1 program [27] was used for Hirschfeld surface analysis of the experimental structure.

4 In Silico Molecular Docking, Druggability and Pharmacokinetics

The crystal structures of the selected protein targets in pdb format were selected from Protein Data Bank (PDB) [Alpha-synuclein (3q25), Rho-kinase (2f2u)]. The ligands attached to the complex proteins were removed and all the polar hydrogen was added, then saved in pdbqt format and used for docking studies. Molecular docking of (4-APH)(4-APH₂)[AsO₄] \cdot H₂O along with arsenic, maltose and 5-(1,4-diazepan-1-sulfonyl)isoquinoline (M77) with human MAOB were investigated using iGEMDOCK (Generic Evolutionary Method for Docking Molecules) [28] on the basis of GEMDOCK pharmacological scoring function [29]. Following, the interactions of the compound with different SARS-CoV-2 virus proteins was realized. We targeted 6LU7, 6M2N, 6M0J and BTF. Crystal structures of spike receptor binding domain of SARS-CoV-2 (PDB 6M0J), was used. For SARS-CoV-2 RNA-dependent RNA polymerase (PDB 7BTF.pdb), cofactors (Zn + 2) in reduced condition were removed. For SARS-CoV-2 3CL protease (3CL pro) (PDB 6M2N.pdb), the novel inhibitor was removed. The crystal structure of COVID-19 main protease (PDB 6LU7) in complex with an inhibitor N3 was also used. All proteins

were preprocessed than targeted for molecular binding with the compound as previously described [30–32]. Preprocessing includes removing water molecules and adding polar hydrogen and Coleman charges [33, 34]. Several biological-related parameters were assessed. The analyses include the lipophilicity, druggability, medicinal chemistry and pharmacokinetics based on ADMET (for absorption, distribution, metabolism, excretion and toxicity) properties as previously described [30, 33].

5 Results and Discussion

5.1 Structure Description

The structure of the title compound Mhadhbi et al. [13], crystallizes in the centrosymmetric triclinic system with P-1 space group; the unit cell parameters are $a = 6.570$ (5) Å, $b = 8.528$ (2) Å, $c = 12.529$ (3) Å, $\alpha = 95.83$ (3)°, $\beta = 97.149$ (4)°, $\gamma = 95.116$ (7)° and $V = 689.2$ (6) Å³. The unit formula (Fig. 1a) is made of two 4-aminopyridinium cations mono and diprotonated ([C₅H₇N₂]⁺, [C₅H₈N₂]²⁺), an arsenate anion [AsO₄]³⁻ and one water molecule. The different components are connected by a network of N/O–H \cdots O hydrogen bonds. In order to find the optimized geometry, theoretical calculations were carried out by the DFT/B3LYP with LanL2DZ and 6–311++ G(d,p) basis sets. The experimental and calculated molecular geometry

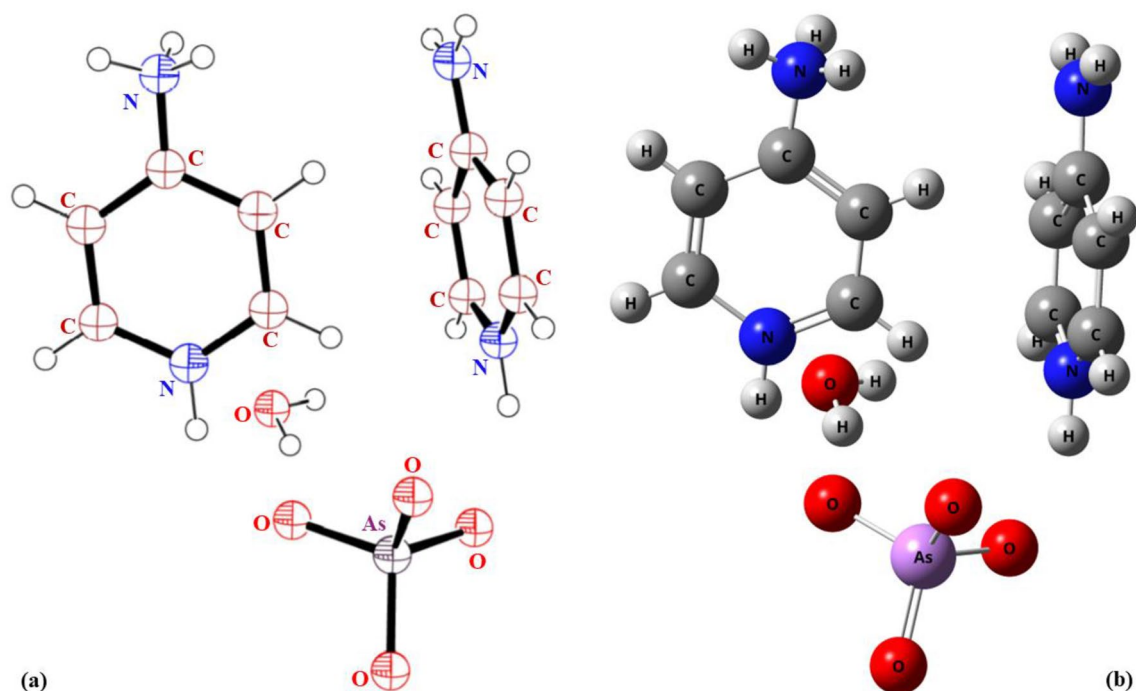


Fig. 1 Asymmetric unit (a) and Optimized geometry (b) of (4-APH)(4-APH₂)[AsO₄] \cdot H₂O

parameters (bond lengths, bond angles of the title compound) were given in Table S1 and Table S2, showing the observed and calculated bond parameters are compatible.

The Fig. 1b represents the corresponding optimized geometry by the DFT calculation. The difference between the optimized and experimental geometries was analyzed in term of Root Mean Square Deviation (RMSD) overlay. The RMSD fits of the bond lengths and bond angles of experimental and calculated geometries are 0.026 Å and 2.946° respectively, which indicate the agreement between the two geometries. As shown in Table S1 and Table S2, a set of calculated geometrical parameters are slightly deviated from the experimental values; this deviation might be due to that fact that the calculations are carried out for a single compound in the gaseous phase and the experimental results are obtained in the solid state.

The details of the molecular bond parameters are briefly summarized below. The experimentally obtained values of the C–N and C–C bond lengths are in the range of 1.311–1.390 and 1.363–1.423 Å, respectively. It can be seen that the N–C and C–C bond lengths predicted by the B3LYP basis are found to be between 1.341–1.472 and 1.373–1.420 Å, respectively. The experimental values of the C–C–C bond angles in the phenyl rings and N–C–C angles vary in the range of 117.038°–120.023° and 117.169°–122.805°, respectively. However, the corresponding theoretical values are in the range of 117.441°–121.309° and 119.303°–122.945°, respectively. As for the anionic group, each arsenic atom at the center of the tetrahedron is connected to four oxygen atoms. The experimental values of the large As–O bond lengths are 1.631–1.651 Å, whereas the theoretical values of the corresponding bond lengths are 1.719–1.828 Å. On one hand, the experimental O–As–O angles vary between 108.239° and 111.234°. These values are in agreement with the theoretical corresponding angles which vary between 100.085° and 115.848°, respectively. The molecular geometry in gas phase may differ from the solid phase owing to the extended hydrogen bonding and stacking interactions (attractive non-covalent interactions between two aromatic rings). The difference between the theoretical and experimental geometry might be to the fact that calculations were performed using isolated molecule in the gaseous phase to obtain theoretical results and in solid state for experimental results. Thus, it is found that most of the optimized bond lengths and the bond angles are in reasonable agreement with the corresponding experimental values. As seen, the calculated geometric parameters represent good approximation and can be used as a foundation to calculate the other parameters for the compound. There are slight differences since the experimental results belong to the solid phase, whereas the calculated values are related to the gas phase.

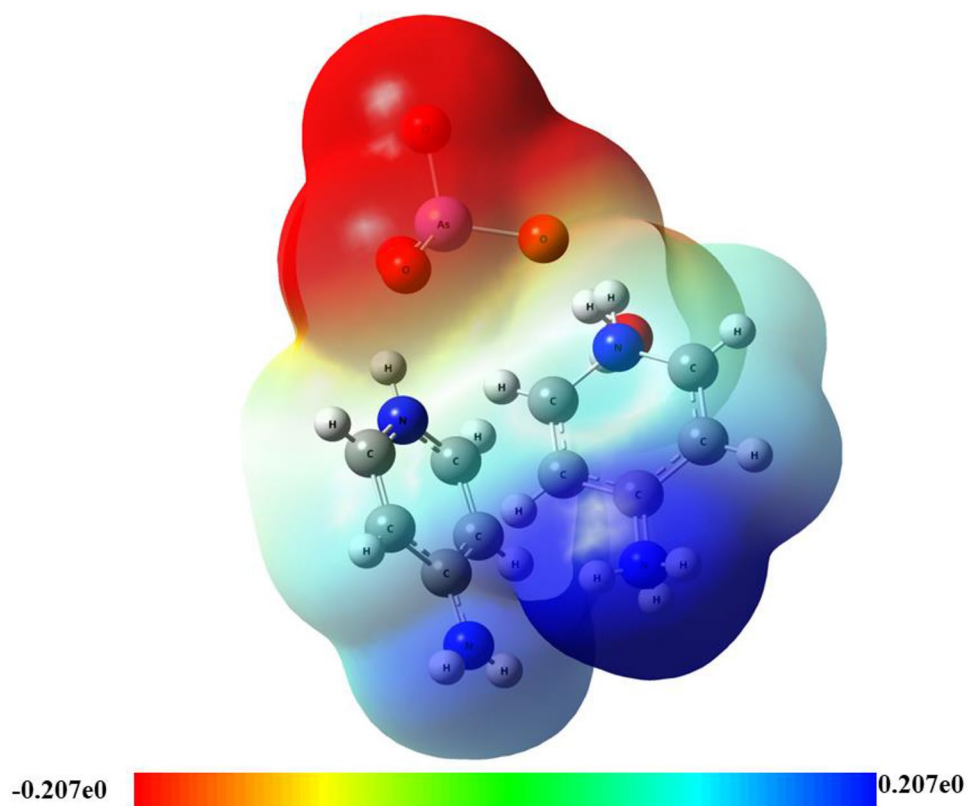
5.2 Molecular Electrostatic Potential Maps

The molecular electrostatic potential (MEP) surface was drawn by the DFT method. The electrostatic potential is used to exhibit the molecular outline, dimension, and electrostatic potential in terms of color grading [34]. The potential is presented in the map of MEP and visualized with different colors as shown in Fig. 2. At DFT level the MEP surface is plotted for the title compound. The color code of these maps ranges from -2.07×10^{-1} (red) and 2.07×10^{-1} a. u. (blue). The mapping represents the donor atoms in blue regions with positive potential; the most positive electrostatic potential (nucleophilic site) is localized hydrogen atoms. The acceptor atoms with negative potential in red regions represent the most electronegative potential (electrophilic sites) and it is mainly localized over anionic group. The green or yellow color indicates the neutral region. This graph shows that the electrophilic sites are located around the hydrogen atoms, whereas the nucleophilic sites are located around the oxygen atoms. MEP surface represents a proof of the creation of hydrogen bond [35]; it is defined as a donor acceptor interaction. The negative region plays an important role in forming a hydrogen bond interaction with the protein. This is well correlated with molecular docking study as well as molecular dynamics study. The electrostatic potential of the donor becomes less negative as the acceptor becomes more negative. The contour map of electrostatic potential confirms that the different negative and positive potential sites of the compound are in accordance with the total electron density surface map.

5.3 Natural Bond Orbital Analysis

A natural bond orbital (NBO) is the calculated bonding orbital with highest electron density. Natural (localized) orbitals are used in computational study to calculate the distribution of electron density in atoms and in bonds in between the atoms. The most important advantage of the NBO method is the information obtained about the interactions in both filled and the virtual orbital which supplement the analysis of both the intra and inter molecular interactions [36]. The strength of the interaction between electron donors and the electron acceptors, or the donating tendency which is from electron donors to electron acceptors and hence the degree of conjugation of the system is measured by the value of energy of the hyperconjugative interactions, $E^{(2)}$. In order to evaluate the donor–acceptor interactions, the second-order Fock matrix was carried out in NBO analysis [37]. For each donor (i) and acceptor (j), the stabilization energy $E^{(2)}$ associated with the delocalization $i \rightarrow j$ is estimated as:

Fig. 2 Molecular electrostatic potential surface (MEPS) map for (4-APH)(4-PH₂)[AsO₄]·H₂O molecule



$$E^{(2)} = \frac{q_i F(i, j)}{(\epsilon_i - \epsilon_j)} \quad (1)$$

where, q_i is the orbital occupancy, ϵ_i and ϵ_j are the diagonal elements and $F(i, j)$ is the off-diagonal NBO Fock matrix element. Table S4 lists the most important second-order perturbation energies and molecular orbital interactions. Here, the strong intermolecular hyper conjugative interactions are observed for the π (C4–C6), π (C9–C11), π (C16–C18) and π (C22–C24) distribute to the anti-bonding orbital of π^* (C4–C6), π^* (C9–C11), π^* (C16–C18), π^* (C22–C24). The other significant interaction is found between Lewis and non-Lewis orbital with oxygen atom lone pairs. The second order energies of the interactions between LP (1) N1, LP (1) N 20 donors to the anti bonding acceptors π^* (C4–C6), π^* (C9–C11), π^* (C16–C18) and π^* (C22–C24). The strong stabilization energy is affected by the intramolecular hyper conjugative interaction between LP (1) N1 and bonding orbital π (C9–C11) which is found to be 119.09 kcal/ mol.

5.4 AIM Approach: Topological Parameters at Bond Critical Points (BCP)

In the AIM theory the nature of the bonding interaction can be determined through an analysis of the properties [38] of the charge density, ρ , and its Laplacian $\nabla^2\rho$, local potential

energy density ($V(r)$), local gradient kinetic energy density ($G(r)$), total energy density ($H(r) = (V(r) + G(r))$) and the bond energy E at the BCPs, and through the properties of the atoms, which are obtained by integrating the charge density over the atom orbitals [38]. In addition, the ellipticity (ϵ) at the BCP is a sensitive index to monitor the π -character of bond. The ϵ is related to λ_1 and λ_2 which correspond to the Eigen values of Hessian and is defined by the relationship: $\epsilon = (\lambda_1/\lambda_2) - 1$. Hence, the AIM graph displaying all the BCPs in the asymmetric unit is presented in Fig. 3. The topological parameters calculated at BCPs are detailed in Table 1. According to the BCP analysis of Table 1 and Based on the Rozas et al. [39] criterion all of the seven hydrogen bonds are considered weak since the Laplacian and the energy density values are positive. The electron density ρ is low and its corresponding Laplacian $\nabla^2\rho$ is positive at all BCPs and are in the range of 0.0040–0.0367 a.u. and 0.0135–0.1217 a.u., respectively. According to Koch and Popelier criteria [40], the hydrogen bonding interaction should have ρ and $\nabla^2\rho$ values within the range 0.0020–0.0400 and 0.0240–0.1390 a.u., respectively. Referring to Table 2, the strongest interaction is found for O₃₁⋯H₂ contact ($\rho = 0.0367$ and $\nabla^2\rho = 0.1217$ a.u.) with an energy that is equal to 41.78 kJ. mol⁻¹. In order to investigate the effect of π -electron delocalization in bonds associated with N and O atoms of N–H⋯O, the analysis of the bond ellipticity is performed. The ellipticities (ϵ) of bond

Fig. 3 AIM molecular graphic showing the different critical points (BCPs) (red small balls) of (4-APH)(4-APH)₂[AsO₄]₂·H₂O

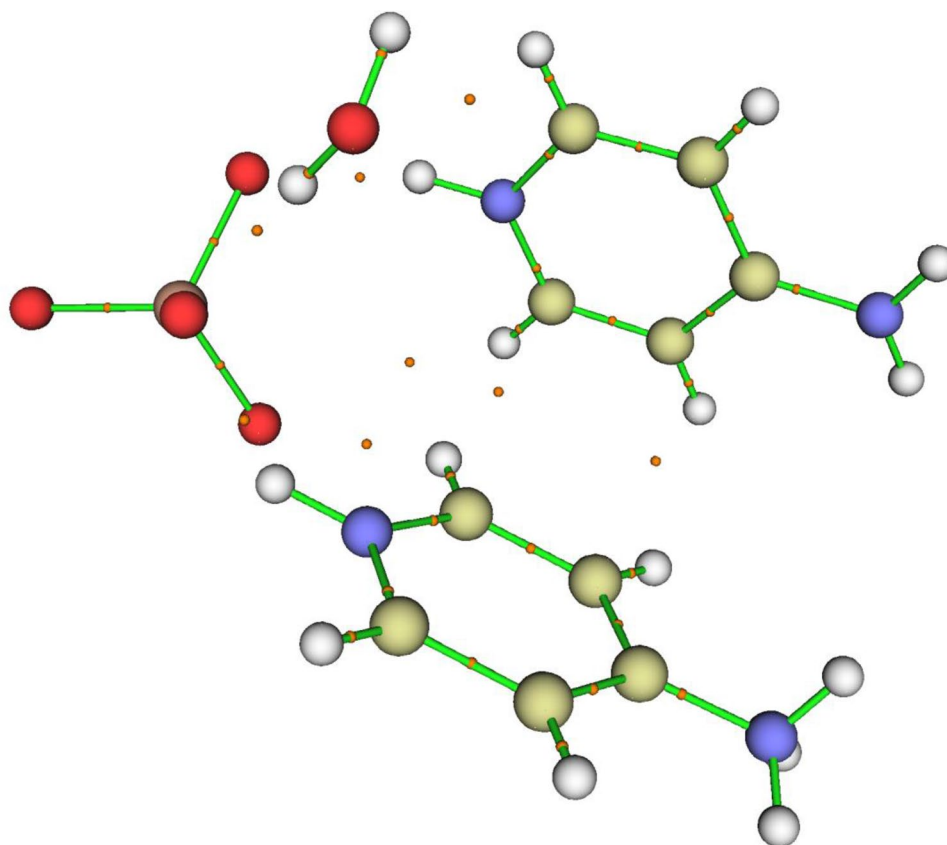


Table 1 Topological parameters (in a.u.) calculated at BCPs: electron density $\rho(r)$, Laplacian of electron density $\nabla^2\rho(r)$, lagrangian kinetic energy density $G(r)$, energy density $H(r)$, electron potential energy density $V(r)$, ellipticity ϵ and estimated interaction energy (E_{int} , in kJ/mol)

BCP	$\rho(r)$	$\nabla^2\rho(r)$	$G(r)$	$H(r)$	$V(r)$	ϵ	$-V(r)/G(r)$	E_{int}
O ₃₅ ...H ₁₂	0.0040	0.0135	0.0026	0.0008	-0.0017	1.629	0.68	-2.25
O ₃₁ ...H ₂	0.0367	0.1217	0.0313	-0.0086	-0.0321	0.037	1.03	-41.78
O ₃₃ ...H ₃₆	0.0311	0.1020	0.0259	-0.0004	-0.0263	0.028	1.02	-34.17
O ₃₂ ...H ₅	0.0047	0.0154	0.0030	0.0089	-0.0021	1.307	0.70	-2.68
O ₃₂ ...H ₁₉	0.0097	0.0327	0.0069	0.0012	-0.0057	0.055	0.82	-7.41
C ₄ ...H ₁₉	0.0049	0.0187	0.0035	0.0012	-0.0023	0.667	0.65	-2.95
C ₆ ...H ₁₇	0.0049	0.0162	0.0031	0.0009	-0.0022	0.258	0.70	-2.83

of aromatic ring at BCP are in range of 0.028–1.629. The ϵ values confirm the presence of resonance assisted intermolecular hydrogen bonds.

5.5 Noncovalent Interaction-Reduced Density Gradient (RDG) Analysis

To prove the existence of weak interactions [41, 42], NCI plots are generated with the plots of the RDG S versus $(\text{sign } \lambda_2)\rho$, where $(\text{sign } \lambda_2)\rho$ is the electron density multiplied by the sign of the second Hessian eigenvalue (λ_2). The value of $(\text{sign } \lambda_2)\rho$ is useful to predict the nature of interaction; for a repulsive interaction $(\text{sign } \lambda_2)\rho > 0$ (steric effect in ring and cage) and for attractive interaction $(\text{sign } \lambda_2)\rho < 0$ (hydrogen bonds). The values close

to zero indicating Van der Waals interactions. To study non-covalent interactions, Johnson et al. [43] developed an approach based on the electronic density and its derivatives named RDG. The RDG were defined using the following equation:

$$RDG(r) = \frac{1}{2(3\pi^2)^{1/3}} \frac{|\nabla\rho(r)|}{(\rho(r))^{4/3}} \quad (2)$$

The strength and nature of interactions can be interpreted from the product $\text{sign } \lambda_2$ times ρ , as blue, green, and red color codes are used to describe stabilizing H-bonding, Van der Waals, as well as destabilizing steric interaction, respectively. The results were collected in Fig. 4a and

Table 2 Global reactivity descriptors and calculated frontier molecular orbital parameters in gas and in solution phase for (4-APH)₂(4-APH₂)[AsO₄]₂·H₂O

Parameter (eV)	Gas	Water
E_{HOMO}	− 6.60366231	− 6.46107458
E_{LUMO}	− 0.801647815	1.4071014
$ E_{HOMO} - E_{LUMO} $ Gap	5.8020	5.0540
Electron affinity (A)	0.801647815	− 1.4071014
Electrophilicity index (ω)	2.3621	0.8250
Ionization potential (I)	6.60366231	6.46107458
Electronegativity (χ)	3.7024	2.5269
Chemical potential (μ)	− 3.7026	− 2.5269
Chemical hardness (η)	2.9010	3.9340
Chemical softness (S)	0.1723	0.1271

The hardness η : $\eta = (I - A)/2$ where A is the ionization potential and I is the electron affinity: $[A = -E_{LUMO}, I = -E_{HOMO}]$, the chemical potential μ : $\mu = -(I + A)/2$; the softness, S: $S = 1/2\eta$; the electronegativity χ : $\chi = (I + A)/2$ and, the electrophilicity index ω : $\omega = \mu^2/2\eta$

illustrate the attractive, Van der Waals and repulsive interactions in the present structure. The NCI-RDG graph of the title compound is plotted in Fig. 4b. The observed red areas (spots) indicate steric repulsions and are localized mostly in the middle of benzene rings. The observed green and blue areas between the organic and the inorganic parts indicate the existence of Van der Waals and steric effects.

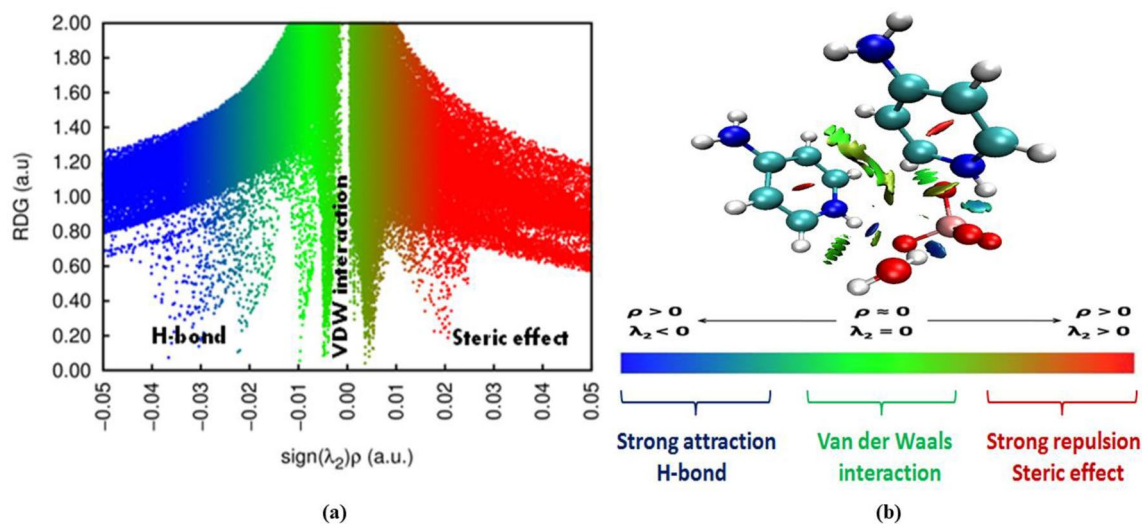
5.6 Frontier Molecular Orbital Analysis

In order to evaluate the energetic behavior [44], we carried out the calculations in gas phase and in solvent. The calculated energy values of HOMO and LUMO are around − 6.60 eV

and 1.40 eV, respectively, in the gas phase and in water. The energies and the pictorial illustration of HOMO, LUMO, HOMO − 1 and LUMO + 1 frontier molecular orbitals are shown in Fig. 5. The brown color refers to the positive phase, which indicates the nucleophilic site. The negative phase is indicated by green color, and is related to the electrophilic site. Accordingly, the energy gap of HOMO–LUMO explains the eventual charge transfer interaction within the compound. Furthermore, in going from the gas phase to the solvent phase, the increasing value of the energy gap and molecule becomes more stable and the low values of frontier orbital gap in (4-APH)₂(4-APH₂)[AsO₄]₂·H₂O make it more reactive. Additionally, a compound with a small frontier orbital gap is readily polarizable and normally exhibits high chemical reactivity and low kinetic stability [45–47]. Furthermore, the global chemical reactivity descriptors (GCRD) are another vital technique to understand the chemical properties of a compound such as chemical hardness (η), chemical potential (μ), chemical softness (S), electronegativity (χ) and electrophilic index (ω). The formula to obtain GCRD is derived from HOMO–LUMO energies, taking the HOMO energy as ionization potential (I) and LUMO as electron affinity (A) and the data are tabulated in Table 2. The concept of these parameters is related to each other [37, 48–50] where:

$$\eta = \frac{E_{LUMO} - E_{HOMO}}{2} \quad (3)$$

$$S = \frac{1}{2\eta} \quad (4)$$

**Fig. 4** Reduced density gradient (a) and isosurface density (b) plot along with the color filled scale bar defining interaction limits of (4-APH)₂(4-APH₂)[AsO₄]₂·H₂O molecule

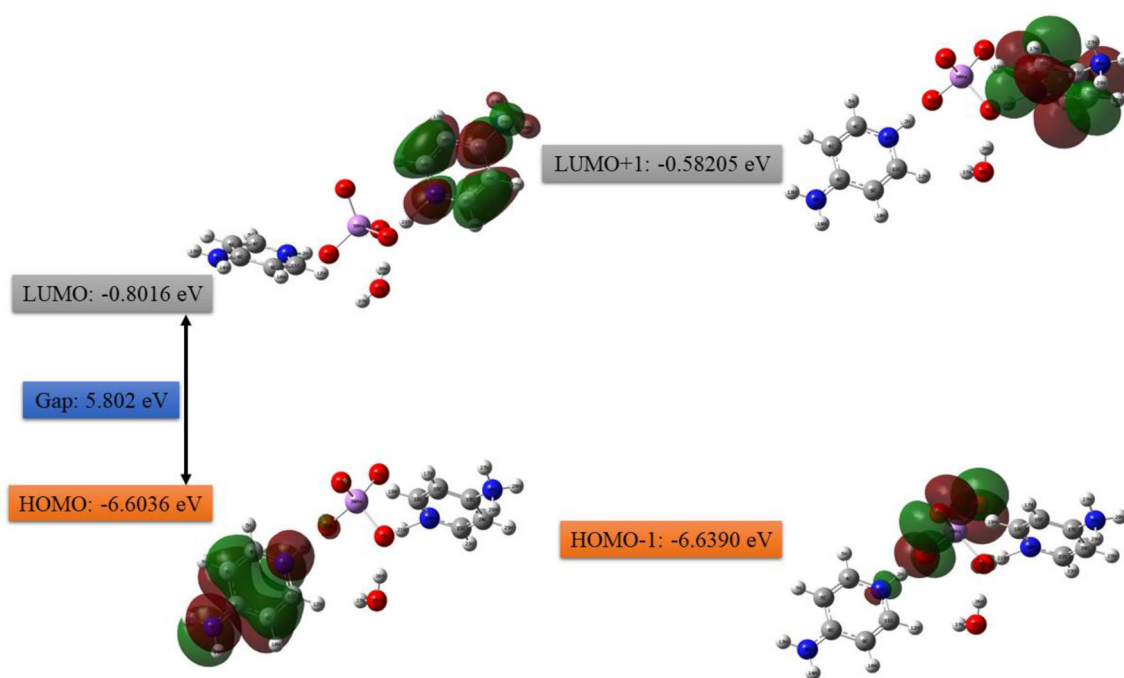


Fig. 5 Plots of the frontier and second frontier molecular orbitals of (4-APH)(4-APH₂)[AsO₄]·H₂O with energies

$$\mu = \frac{E_{LUMO} + E_{HOMO}}{2} \quad (5)$$

$$\chi = \frac{I + A}{2} \quad (6)$$

$$\omega = \frac{\mu^2}{2\eta} \quad (7)$$

Using the above equations, the chemical potential, hardness and electrophilicity index have been calculated and their values are shown in Table 2. The ionization potential value indicates that energy of 6.60 eV in gas phase is required to remove an electron from the HOMO. The lower value of electron affinity shows higher molecular reactivity with the nucleophiles. Higher hardness and lower softness values confirm the higher molecular hardness associated with the compound. The electrophilicity index helps in describing the biological activity of the compound.

5.7 Nonlinear Optical Parameters

The application of (4-APH)(4-APH₂)[AsO₄]·H₂O in the field of nonlinear optics was investigated through the hyperpolarizability calculation by analyzing the vibrational modes of the optimized molecular geometry. The calculated values of dipole moment, polarizability and first

order hyperpolarizability and their components in gas phase and water solvent are listed in Table 3. However, the values of α and β from Gaussian output are given in atomic units (a.u.) and converted into electronic units (esu) (α : 1 a.u. = 0.1482×10^{-24} esu, β : 1 a.u. = 8.6393×10^{-33} esu). The dipole moment (μ) and first order hyperpolarizability (β) are found to be 39.1985 Debye and 22.052×10^{-31} esu, respectively. According to the NLO results, the crystal has a total dipole moment of 28.54 times greater than that of urea. The first order hyperpolarizability is more than 5.91 times greater than that of urea (μ and β of urea are 1.3732 Debye and 3.728×10^{-31} esu) and 3.22 times that of the reference crystal KDP ($\beta_{\text{KDP}} = 6.85 \times 10^{-31}$ esu) [51]. In addition, it is associated with intra-molecular charge transfer that is attributed to electron cloud movement through π -conjugated framework from electron donor to electron acceptor groups. Therefore, the components of hyperpolarizability are useful to understand charge delocalization in the compound. The maximum charge delocalization occurs along β_{xxx} in the molecule under investigation. According to this result, this compound may exhibit excellent nonlinear optical properties.

5.8 Thermodynamic Analysis

The computed parameters were summarized in Table 4. On the basis of vibrational analysis at B3LYP/6-31G (d, p), the standard statistical thermodynamic functions: heat capacity $C_{p,m}^0$, entropy S_m^0 and enthalpy change H_m^0 for the

Table 3 The calculated electric dipole moment μ (D) the average polarizability α ($\times 10^{-24}$ esu) and the first hyperpolarizability β ($\times 10^{-31}$ esu) for the ((4-APH)(4-APH₂)[AsO₄]-H₂O)

Parameters	In gas phase	In water	Parameters	In gas phase	In water
μ_x	- 8.2917	20.8079	β_{xxx}	20.619	6.759
μ_y	2.2315	32.9977	β_{xxy}	22.911	- 22.682
μ_z	5.4462	- 3.8353	β_{xyy}	11.613	17.642
μ (D)	10.168234	39.198551	β_{yyy}	15.567	- 4.517
α_{xx}	27.214	38.347	β_{xxz}	8.913	- 3.503
α_{xy}	1.248	- 3.005	β_{xyz}	2.476	- 3.381
α_{yy}	29.307	29.658	β_{yyz}	- 1.114	12.141
α_{xz}	- 2.189	3.902	β_{xzz}	1.962	- 9.125
α_{yz}	3.684	- 0.017	β_{yzz}	4.962	11.929
α_{zz}	21.080	32.997	β_{zzz}	5.353	- 4.191
α (esu)	25.867	33.667	β (esu)	56.826	22.052

Bold values indicate the total value of the parameters

However, α and β values of the Gaussian output are in atomic units (a.u.), so they have been converted into electronic units (esu) (α ; 1 a.u. = 0.1482×10^{-24} esu, β ; 1 a.u. = 8.6393×10^{-33} esu)

Table 4 Calculated thermodynamic parameters (at 298.15 K) for ((4-APH)(4-APH₂)[AsO₄]-H₂O) with DFT method

Thermodynamic parameters	Gas	Water
SCF energy E (u.a)	- 992.52725	- 992.61229
Zero-point vibrational energy (kcal mol ⁻¹)	179.74496	180.05624
Rotational constants (GHz)		
A	0.23361	0.38219
B	0.19277	0.10311
C	0.12348	0.09282
Thermal energy (kcal mol ⁻¹)	194.047	194.956
Specific heat at constant volume C _v (cal mol ⁻¹ K ⁻¹)	82.765	82.949
Entropy S (cal mol ⁻¹ K ⁻¹)	165.65	174.617
Dipole moment (Debye)	10.168234	39.198551

title compound were calculated within the temperature range from 100 to 1000 K and as observed in Table S4. From Fig. S1, it can be observed that these thermodynamic functions are increasing with temperature due to the fact that the molecular vibrational intensities increase with temperature [52]. The correlation equations between the thermodynamic functions and temperatures were fitted by quadratic formulas, and R is the corresponding fitting factors (R^2) for the thermodynamic properties. The corresponding R^2 fitting factor of each thermodynamic quantities $C_{p,m}^0$, S_m^0 , and H_m^0 are 0.99956, 0.9998 and 0.99955, respectively. The corresponding fitting equations between thermodynamic properties and temperature are as follows:

$$C_{p,m}^0 = 57.73802 + 1.14384T - 5.10116 \times 10^{-4}T^2 \quad (8)$$

$$S_m^0 = 295.48957 + 1.44264T - 4.09224 \times 10^{-4}T^2 \quad (9)$$

$$H_m^0 = -17.75073 + 0.19291T + 2.8839 \times 10^{-4}T^2 \quad (10)$$

All the thermodynamic data afford helpful information for the study of thermodynamic energies and estimate directions of chemical reactions according to the second law of thermodynamics in thermochemical field [53]. Please note that all thermodynamic calculations were done in gas phase and they could not be used in solution.

5.9 Hirshfeld Surface Analysis

The molecular Hirshfeld surface [23, 54, 55]: d_{norm} , shape index, curvedness, d_e and d_i for the title compound are illustrated in Figs. S2 (a–e) and mapped over: d_{norm} ranges (- 0.632 to 1.120 Å), shape index ranges (- 1.000 to 1.000 Å), curvedness (- 4.000 to 0.400 Å), d_e ranges (0.718 to 2.411 Å) and d_i ranges (0.719 to 2.430 Å), respectively. The examination of the full distribution of intermolecular interactions is shown in 2D map fingerprint plots (Fig. 6). The asymmetric property of the compound is due to the hydrogen bonds and the intermolecular interactions within the crystal. The 2D fingerprints (Fig. 6a) show that the intermolecular, O...H and

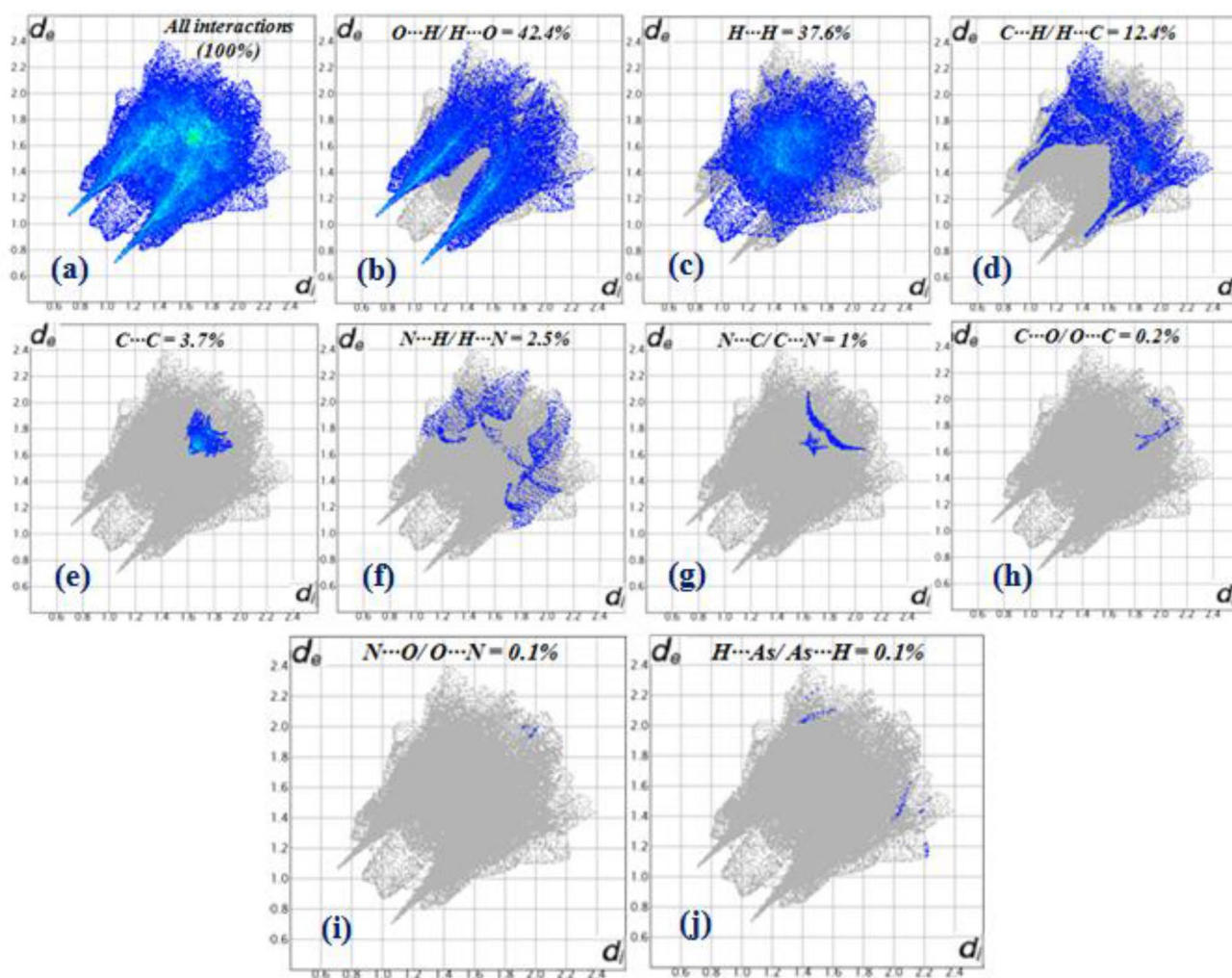


Fig. 6 2D fingerprint plots of (4-APH)(4-APH₂)[AsO₄] \cdot H₂O compound

H \cdots H interactions are the dominant contacts. Figure 6b represents the O \cdots H/ H \cdots O contacts between the hydrogen atoms located inside the Hirshfeld surface and the oxygen atoms characterized by two symmetrical points located at the top left and right. The largest contribution to the total Hirshfeld area is about (42.4%). Figure 6c illustrates the interaction H \cdots H. The contribution to the surface Hirshfeld about (37.6%) in the surface grouped points which occupy half of surface. Figure 6d shows the interaction between groups C \cdots H/ H \cdots C. These interactions have a contribution to the surface Hirshfeld of (12.4%). The contribution of other intermolecular interactions is found to be in decreasing order: [C \cdots C (3.7%), N \cdots H (2.5%), N \cdots C (1%), C \cdots O (0.2%), N \cdots O (0.1%) and H \cdots As (0.1%)]. Fig. S3 summarized the distribution of

individual intermolecular interactions on the basis of HS analysis for the title compound.

5.10 Vibrational Studies

The experimental and theoretical FT-IR and FT-Raman spectra were shown in Figs. 7, 8, respectively. Theoretically computed frequencies with their relative intensities, probable assignments and potential energy distribution (PED) are summarized in Table S5. To the assignments, only potential energy distributions (PED) contributions $\geq 10\%$ and the experimental IR spectrum were considered. The theoretical intensities show slight deviations from the experimental values since the theoretical wavenumbers are obtained from the isolated molecule in the

Fig. 7 Superposition of the experimental (red) and the DFT computed (blue) FT-IR spectra of (4-APH)(4-APH₂) [AsO₄]₂·H₂O in the 400–4000 cm⁻¹ region

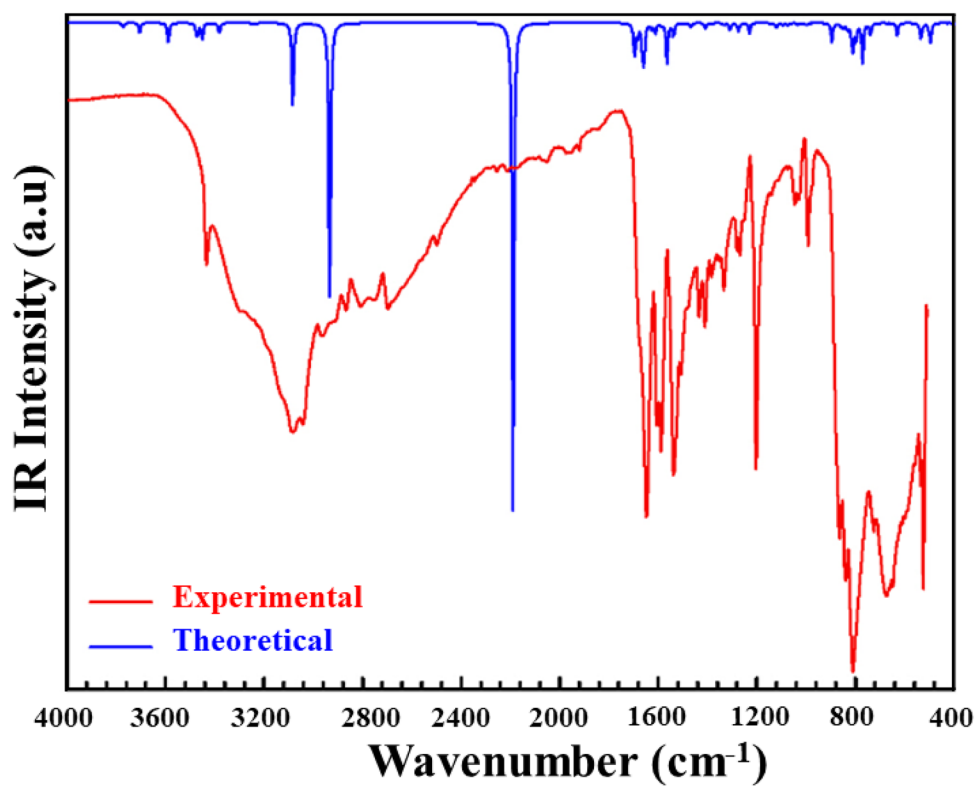
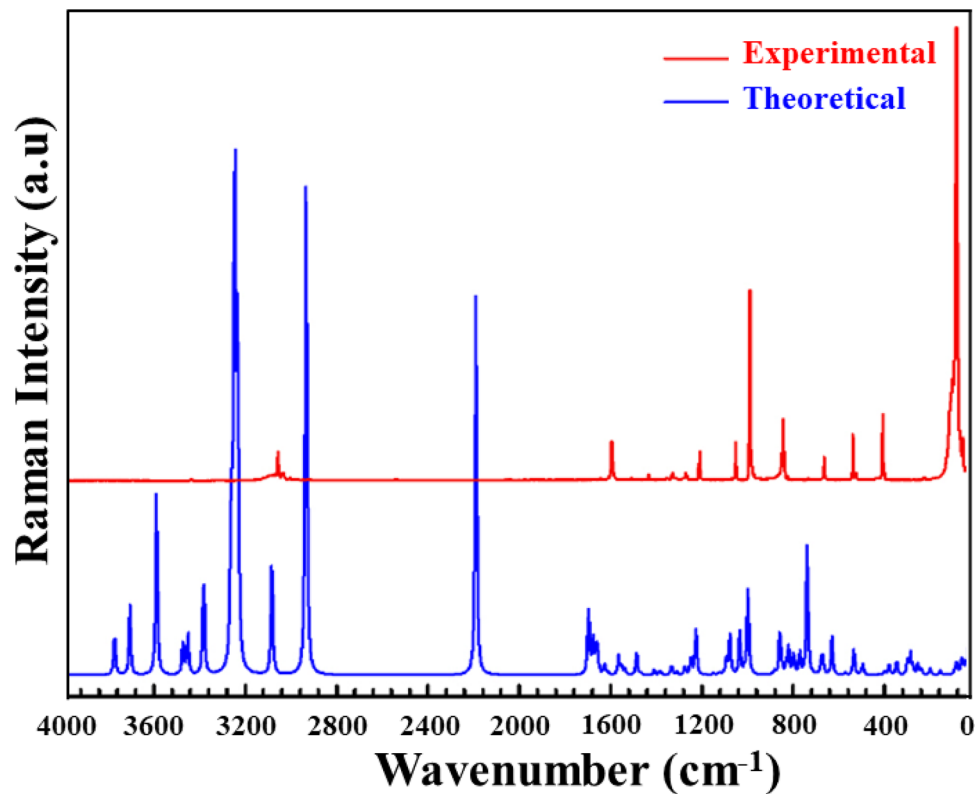


Fig. 8 Superposition of the experimental (red) and the DFT computed (blue) FT-Raman spectra of (4-APH)(4-APH₂) [AsO₄]₂·H₂O in the 0–4000 cm⁻¹ region



gaseous phase and the experimental wavenumbers are obtained from the isolated molecule in solid state.

5.10.1 Arsenate Groups Vibrations

According to the literature, the isolated arsenate anion $[\text{AsO}_4]^{3-}$ with Td point group symmetry led to four Raman active normal modes: $\nu_1(A_1)$, $\nu_2(E)$, $\nu_3(F_2)$ and $\nu_4(F_2)$ with average wavenumbers 837, 349, 887 and 463 cm^{-1} , respectively [56]. ν_1 and ν_3 involve the symmetric and the asymmetric stretching mode of the As–O bond, whereas ν_2 and ν_4 involve mainly O–As–O symmetric and asymmetric bending modes. We have distinguished the four fundamental modes (ν_1 , ν_2 , ν_3 and ν_4) of the $[\text{AsO}_4]^{3-}$ anion in the wave number region from 300 to 1000 cm^{-1} . In the region, the $[\text{AsO}_4]^{3-}$ stretching and bending vibrations expected to appear, as well as the modes associated with the internal modes of the organic cations. The band at 850 cm^{-1} in Raman spectrum is assigned to the asymmetric stretching ν_3 mode of the arsenate ion. In IR spectrum, this mode also appears as a single band at 865 cm^{-1} (with PED contribution of 93%). The band related to the symmetric stretching mode ν_1 vibration is located at 817 cm^{-1} in the IR spectrum while in the Raman spectrum it is absent. The bands concerned with the asymmetric and symmetric bending vibration ν_4 and ν_2 of the arsenate ion are identified in the $550\text{--}700\text{ cm}^{-1}$ and $300\text{--}450\text{ cm}^{-1}$ frequency regions respectively. The very strong band observed in the Raman spectrum at 667 cm^{-1} and the strong band at 677 cm^{-1} in the IR spectrum can be easily assigned to ν_4 mode (with PED contribution of 88%). The same bending vibration is predicted at 665 and 677 cm^{-1} respectively, by DFT method. The symmetric mode ν_2 appears in the Raman spectrum as a shoulder band at 410 cm^{-1} . This mode is theoretically calculated at 374 cm^{-1} by DFT method. As seen from Table S5, all modes associated to the arsenate's groups are well reproduced by theoretical method.

5.10.2 C–H Vibrations

Heterocyclic aromatic compounds and its derivatives are structurally very close to benzene. The C–H stretching frequency of such compounds falls very nearly in the region $3000\text{--}3100\text{ cm}^{-1}$ which is the characteristic region for the ready identification of C–H stretching vibrations. Hence, the both FT-IR and FT-Raman bands were observed at 3095 cm^{-1} and 3059 cm^{-1} assigned to CH asymmetric stretching. It is noticeable that asymmetric stretching vibrations occurred at higher wave number. The theoretically calculated harmonic wavenumber

at 3230 cm^{-1} and 3094 cm^{-1} in B3LYP/6-31G(d,p) basis set respectively with PED contribution of 86%.

5.10.3 N–H Vibrations

Generally, NH stretching modes cause to vibrational bands in absorption region above $3000\text{--}3500\text{ cm}^{-1}$. This band in the FT-IR spectrum is observed at 3432 cm^{-1} , but the mode is not observed Raman spectra of the compound. The theoretically calculated harmonic wavenumber at 3452 cm^{-1} and 3307 cm^{-1} in B3LYP/6-31G(d,p) basis set respectively with PED contribution of 97%. On the other hand, the NH_2 in plane bending (scissoring) mode are observed as an individual band at $1592\text{--}1602$ (IR-Raman). The theoretically calculated harmonic wavenumber at 1627 cm^{-1} and 1599 cm^{-1} in B3LYP/6-31G(d,p) basis set respectively with PED contribution of 89%.

5.10.4 C=C Vibrations

The C=C skeletal stretching vibrations in aromatic rings generally appear at $1430\text{--}1625\text{ cm}^{-1}$ [57, 58]. While the C=C stretching modes in the benzene rings of the compound are observed at 1436 cm^{-1} in FT-IR and 1435 cm^{-1} in FT-Raman spectra. The wavenumber values calculated for these C=C vibrations are calculated at 1467 and 1442 cm^{-1} with 45% contributions of PED, respectively. Also, it is observed at 1648 cm^{-1} in FT-IR spectrum. The theoretically calculated harmonic wavenumber at 1697 and 1668 cm^{-1} with B3LYP/6-31G(d,p) basis sets in both FT-IR and FT-Raman spectra respectively.

5.10.5 C–N Vibrations

The identification of C–N stretching modes in the side chains is a rather difficult task since there are problems in identifying these frequencies from other vibrations. The vibrational bands observed at 1336 and 1332 cm^{-1} in FT-IR and FT-Raman spectra are assigned to C–N vibrations. The theoretically calculated harmonic wavenumber at 1333 and 1310 cm^{-1} respectively with PED contribution of 56%. Additionally, the C–NH and C– NH_2 stretching band are observed at 1040 and 1057 cm^{-1} in IR and Raman spectra. The wavenumber values calculated for these CN vibrations are calculated at 1074 and 1057 cm^{-1} with 67% contributions of PED, respectively.

5.10.6 O–H Vibrations

At high wavenumbers, the IR and Raman spectra show an absorption band centered at 3042 and 3036 cm^{-1} , respectively, which is assignable to the stretching vibration mode of water molecules (O–H). The theoretically computed

values using DFT calculations are 3083 cm^{-1} and 2954 cm^{-1} (with PED contribution of 91%) are in good agreement with the experimental values.

5.11 Molecular Docking Simulation, Druggability and Pharmacokinetics

The binding interactions of the ligand with the target protein or enzyme are generally through intermolecular bonds [33]. This method is crucial in drug design and it's is frequently the preferred way for estimating the bioactive conformation of the ligand in the protein binding region [59, 60]. Using

iGEMDOCK program, we can determine the interaction energy of a ligand with a protein (also called free energy binding). Generally, this interaction energy is not found from a single structure. In fact, it corresponds to the average energy of several stable structures. The results reveal four docked poses, so four energy values. The best position that has the lowest energy corresponds to the most stable protein/ligand complex [61, 62]. Docking calculations of interaction energies were subsequently clustered in Table 5. Figure 9 represents the molecular docking of Alpha-synuclein protein (3q25) with the two ligands that are Aresnic and Maltose. Molecular docking led to the following results: the

Table 5 Molecular docking results of interaction energies in kcal/mol using iGEMDOCK

Protein molecule	Ligand molecule	Total energy	VDW	H-bond	Electronic	AverConPair
Alpha-synuclein (3q25)	Aresnic	− 93.6683	− 60.3684	− 33.2999	0	26.15
	MALTOSE	− 107.384	− 55.243	− 52.1406	0	26.3043
Rho-kinase (2f2u)	Aresnic	− 92.187	− 66.9125	− 25.2745	0	26.75
	5-(1,4-Diazepan-1-sulfonyl) isoquinoline (M77)	− 95.4741	− 75.5128	− 19.9613	0	28.2

Fig. 9 Localization of the best docked poses for: Aresnic (a) and Maltose (b) of Alpha-synuclein protein estimated via accurate docking in by iGEMDOCK

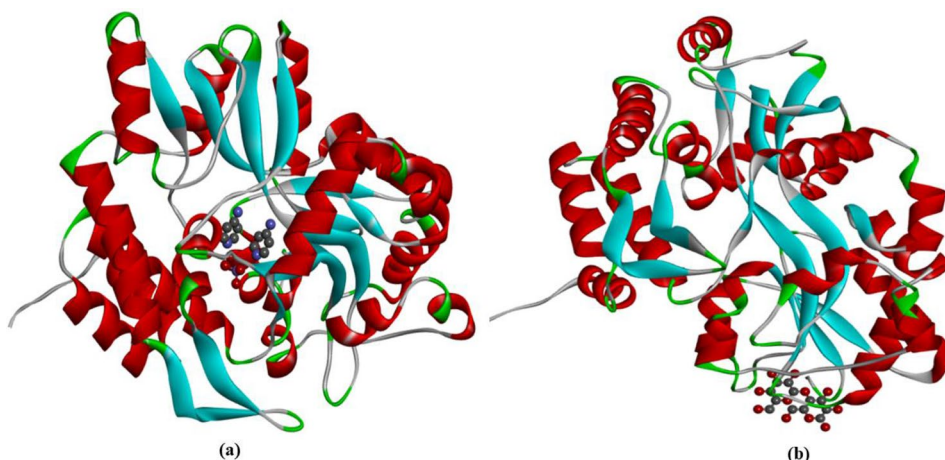
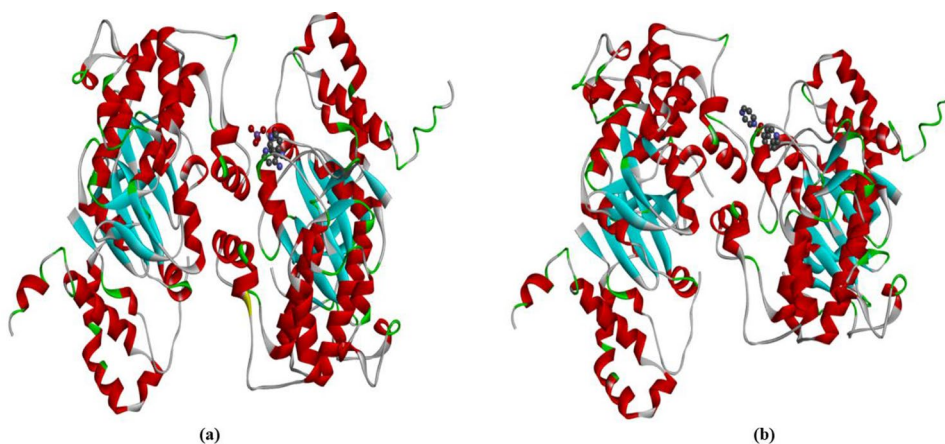


Fig. 10 Molecular docking of Rho-kinase protein with the ligands Aresnic (a) and 5-(1,4-diazepan-1-sulfonyl) isoquinoline (M77) (b) estimated via accurate docking in by iGEMDOCK



total energies equal to -93.6683 and -107.384 kcal/mol for Aresnic and Maltose interacting with Alpha-synuclein protein, respectively. Likewise, for Alpha-synuclein protein, the Maltose ligand is the strongest binding since it possesses the strongest energy (in absolute value) -107.384 kcal/mol, the van der Waals interaction -55.243 kcal/mol, the strongest averconpair 26.3043 kcal/mol and H-bond interaction -52.1406 kcal/mol. The ligand Aresnic is found with energy equal to -93.6683 kcal/mol. Following the previous observations, a new protein was studied called Rho-kinase (2f2u) in interaction with the following Ligand: Aresnic and 5-(1,4-diazepan-1-sulfonyl) isoquinoline (M77). Localization of the best docked poses of these complexes estimated via docking calculations is given in Fig. 10. Table 5 analysis shows that our compound 5-(1,4-diazepan-1-sulfonyl) isoquinoline takes the highest energy value which is equal to -95.4741 kcal/mol, also it presents the strongest van der Waals interaction -75.5128 kcal/mol) and averconpair 28.2 kcal/mol. According to the docking results, the interactions observed between Alpha-synuclein (and also between Rho-kinase) with the Aresnic ligand show the good efficacy of inhibition of the studied compound, indicating that they are promising inhibitors in the treatment of Alzheimer's diseases and in general way of psychic diseases. Later on, the antiviral potential of the compound was assessed. Four different proteins were targeted: 6LU7, 6M0J, 6M2N and 7BTF. The binding affinities of the complex, its interaction bonds, the closest interacting residues and the distance to closest interacting residues are shown in Table 6. The results showed negative binding energies ranging from -3.1 to -4.1 kcal/mol and up to five conventional hydrogen bonds, particularly with 6LU7, which is the SARS-CoV-2 main protease [61, 63]. The latter is highly involved in SARS-CoV-2 inducing COVID-19 pathogenesis and even its complication with acute respiratory distress syndrome, which might lead to death [63]. Regarding the measure of the distance to the closest interaction residue, it has been predicted that it ranges between 2.267 Å to 2.714 Å for 6M0J and 6LU7 respectively, which suggest that the compound is strongly embedded in the different protein pocket regions. These data

Table 7 Lipophilicity, druglikeness, medicinal chemistry and pharmacokinetics of the novel organic arsenate templated by 4-aminopyridine compound

Entry	(4-APH) (4-APH ₂) [AsO ₄]-H ₂ O
<i>Lipophilicity and druglikeness</i>	
Consensus Log P_{ow}	0.62
Bioavailability Score	0.17
<i>Medicinal chemistry</i>	
PAINS	0 alert
Leadlikeness	0 alert
Synthetic accessibility	3.85
<i>Pharmacokinetics</i>	
Gastro-intestinal absorption	Low
BBB permeant	No
P-gp substrate	Yes
CYP1A2 inhibitor	No
CYP2C19 inhibitor	No
CYP2C9 inhibitor	No
CYP2D6 inhibitor	No
CYP3A4 inhibitor	No
Log Kp (skin permeation)	-10.51 cm/s

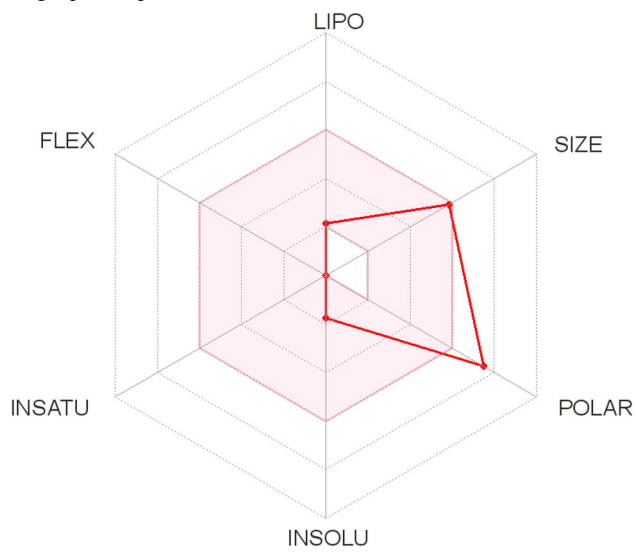


Table 6 Ligand and proteins (6LU7, 6M0J, 6M2N and 7BTF) interactions: binding affinities, bonds, closest interacting residues and distance to closest interacting residues

Ligand and proteins	6LU7	6M0J	6M2N	7BTF
Binding energy (kcal/mol)	-3.1	-3.7	-4.1	3.9
Hydrogen bonds (residues)	5 (2×Phe185, Gly179, Asn180, Cys85)	2 (Ile410, Tyr380)	3 (Thr26, 3WL401, His41)	4 (Pro677, Glu350, 2×His347)
Electrostatic interactions (residues)	–	–	–	1 (Arg349)
Hydrophobic interactions (residues)	–	2 (Thr376, Lys378)	3 (2×3WL401, Leu27)	1 (Arg349)
No. closest interacting residues	6	4	4	4
Distance to closest interacting residues (Å)	2.714	2.267	2.273	2.513

prove that the compound filled well into the pocket region of the targeted proteins and established conventional hydrogen bonds, electrostatic and hydrophobic bonds, which satisfactory support the potential biological effect of the compound, particularly its antiviral effect as compared with previous published reports [62, 63]. In fact, it has been reported that several biological and synthesized compounds possessed potential ameliorative effect against SARS-CoV-2 inducing COVID-19 [62–64]. To rationalize these results and the possible use of its novel organic arsenate templated by 4-aminopyridine compound, its lipophilicity, druggability, medicinal chemistry and pharmacokinetics were assessed. The findings are shown in Table 7. The compound showed acceptable consensus Log Po/w and bioavailability score (0.97). While its absorption via both the gastro-intestinal tract and the skin were low (Log Kp = -10.51 cm/s), it was not categorized as blood–brain–barrier (BBB) permeant but it was a substrate of the p-glycoprotein. Cytochrome P450 (CYP) isoforms, such as CYP1A2, CYP2C19, CYP2C9, CYP2D6 and CYP3A4, are commonly used in biotransformation of drugs and xenobiotics [30, 33, 61]. In this study, the screened CYP enzyme isoforms data indicate that the compound is inhibiting none of these isoenzymes. Thus, suggesting promising pharmacokinetic properties.

6 Conclusion

The optimized molecular structures, vibrational frequencies and corresponding vibrational assignments, Molecular docking and TD/ DFT calculations of ((4-APH)(4-APH₂)[AsO₄]-H₂O) compound have been carried for the first time using B3LYP/6–311++ G(d,p) method. Comparison of the experimental and calculated spectra of the molecule showed that DFT-B3LYP method is in good agreement with experimental data. Besides, MEP surfaces and contours of the compound have also been plotted. In addition to this, the Hirshfeld surface analysis and finger print plots were examined to understand the occurrence of molecular interaction within the molecule. However, according to the DFT calculations, NBO analysis provides an efficient method for studying inter and intramolecular interactions in molecular system. The non-covalent interactions were studied through AIM and RDG analysis. Similarly, the HOMO and LUMO energies were calculated and the energy gap was determined as 5.802 eV in gas phase. Furthermore, NLO behavior of the compound has been explored by calculation of dipole moment and first order hyperpolarizability. Hence, the thermodynamic properties of the title compound were calculated for different temperatures, and the correlations among the properties and temperatures were obtained. Interestingly, the

molecular docking of title compound suggests that it can bind and inhibit the receptor enzymes.

Supplementary Information The online version contains supplementary material available at <https://doi.org/10.1007/s42250-023-00620-8>.

Declarations

Conflict of interest The authors declare that they have no conflict of interest.

References

- Saparov B, Mitzi DB (2016) Chem Rev 116:4558. <https://doi.org/10.1021/acs.chemrev.5b00715>
- Jin J, Jia M-J, Wang YC, Yu JH, Yang QF, Xu JQ (2011) Inorgan Chem Commun 14:1681. <https://doi.org/10.1016/j.inoche.2011.07.006>
- Edwards K, Herringer SN, Parent AR, Provost M, Shortsleeves KC, Turnbull MM, Dawe LN (2011) Inorgan Chem Acta 368:141. <https://doi.org/10.1016/j.ica.2010.12.070>
- Jin Y, Yu CH, Wang WX, Li SC, Zhang W (2014) Inorgan Chem Acta 413:97. <https://doi.org/10.1016/j.ica.2014.01.005>
- Staskiewicz B, Czupinski O, Czapla Z (2014) J Mol Struct 1074:723. <https://doi.org/10.1016/j.molstruc.2014.05.036>
- Zhu X-H, Mercier N, Frère P, Blanchard P, Roncali J, Allain M, Pasquier C, Riou A (2003) Inorg Chem 42:5330. <https://doi.org/10.1021/ic034235y>
- Lu DF, Di YY, He DH (2013) Renew Energy 50:498. <https://doi.org/10.1016/j.renene.2012.07.016>
- Guo L, Xu S, Zhao G, Liu H (2012) J Phys Chem Solids 73:688. <https://doi.org/10.1016/j.jpcs.2012.01.007>
- Englert U (2010) Coord Chem Rev 254:537. <https://doi.org/10.1016/j.ccr.2009.08.007>
- Guloy AM, Tang ZJ, Miranda PB, Srdanov VI (2001) Adv Mater 13:833. [https://doi.org/10.1002/1521-4095\(200106\)13:11%3c833::AID-ADMA833%3e3.0.CO;2-T](https://doi.org/10.1002/1521-4095(200106)13:11%3c833::AID-ADMA833%3e3.0.CO;2-T)
- Baoub L, Jouini A (1998) J Solid State Chem 141:343. <https://doi.org/10.1006/jssc.1998.7933>
- Rayes A, Ben Nasr C, Rzaigui M (2004) Mater Res Bull 39:1113. <https://doi.org/10.1016/j.materresbull.2004.02.017>
- Mhadhbi N, Naïli H, Jarraya K (2017) Phys E 87:171. <https://doi.org/10.1016/j.physe.2016.11.028>
- Issaoui N, Ghalla H, Brandan SA, Bardak F, Flakus HT, Atac A, Oujia B (2017) J Mol Struct 1135:209. <https://doi.org/10.1016/j.molstruc.2017.01.074>
- Gatfaoui S, Issaoui N, Roisnel T, Marouani H (2019) J Mol Struct 1191:183. <https://doi.org/10.1016/j.molstruc.2019.04.093>
- Frisch MJ et al (2009) GAUSSIAN 09, Revision A.02. Gaussian, Inc., Wallingford
- Becke AD (1996) J Chem Phys 104:1040. <https://doi.org/10.1063/1.470829>
- Lee C, Yang W, Parr RG (1988) Phys Rev B 37:785. <https://doi.org/10.1103/physrevb.37.785>
- Hay PJ, Wadt WR (1985) J Chem Phys 82:299. <https://doi.org/10.1063/1.448975>
- Dennington R, Keith T, Millam J (2009) GaussView, Version 5. Semichem Inc., Shawnee Mission
- Glendening ED, Badenhoop JK, Reed AD, Carpenter JE, Weinhold F (1996) NBO 3.1. Theoretical Chemistry Institute, University of Wisconsin, Madison

22. Kansız S, Azam M, Dege N, Ermiş N, Al-Resayes SI, Alam M (2022) *Green Chem Lett Rev* 15:825. <https://doi.org/10.1080/17518253.2022.2130016>
23. Azam M, Sahoo PK, Mohapatra RK, Kumar M, Ansari A, Moon IS, Chutia A, Al-Resayes SI, Biswal SK (2022) *J Mol Struct* 1251:132039. <https://doi.org/10.1016/j.molstruc.2021.132039>
24. Kansız S, Tolan A, Azam M, Dege N, Alam M, Sert Y, Al-Resayes SI, İçbudak H (2022) *Polyhedron* 218:115762. <https://doi.org/10.1016/j.poly.2022.115762>
25. Azam M, Velmurugan G, Trzesowska-Kruszynska A, Al-Resayes SI, Kruszynski R, Venuvanalingam P (2022) *Inorgan Chim Acta* 534:120807. <https://doi.org/10.1016/j.ica.2022.120807>
26. Lu T, Chen F (2012) *J Comput Chem* 33:580. <https://doi.org/10.1002/jcc.22885>
27. Turner M, McKinnon J, Wolff S, Grimwood D, Spackman P, Jayatilaka D, Spackman M (2017) *CrystalExplorer17*. University of Western Australia, Crawley, p 491
28. Yang JM, Chen CC (2004) *Proteins Struct Funct Bioinform* 55:288. <https://doi.org/10.1002/prot.20035>
29. Yang JM, Shen TW (2005) *Proteins Struct Funct Bioinform* 59:205. <https://doi.org/10.1002/prot.20387>
30. Mohapatra RK, Dhama K, El-Arabey AA, Sarangi AK, Tiwari R, Emran TB, Azam M, Al-Resayes SI, Raval MK, Seidel V, Abdalla M (2021) *J King Saud Univ Sci* 33:101637. <https://doi.org/10.1016/j.jksus.2021.101637>
31. Abdalla M, Mohapatra RK, Sarangi AK, Mohapatra PK, Eltayb WA, Alam M, El-Arabey AA, Azam M, Al-Resayes SI, Seidel V, Dhama K (2021) *J Saudi Chem Soc* 25:101367. <https://doi.org/10.1016/j.jscs.2021.101367>
32. Boufissiou A, Abdalla M, Sharaf M, Al-Resayes SI, Imededdine K, Alam M, Yagi S, Azam M, Yousfi M (2022) *J Saudi Chem Soc* 26:101473. <https://doi.org/10.1016/j.jscs.2022.101473>
33. Badraoui R, Rebai T, Elkahoui S, Alreshidi M, Veettil VN, Noumi E, Al-Motair KA, Aouadi K, Kadri A, De Feo V, Snoussi M (2020) *Antioxidants* 9:1003. <https://doi.org/10.3390/antiox9101003>
34. Sagaama A, Noureddine O, Brandan SA, Jedryka AJ, Flakus HT, Ghalla H, Issaoui N (2020) *Comput Biol Chem* 87:107311. <https://doi.org/10.1016/j.compbiolchem.2020.107311>
35. Mohan N, Suresh CH (2014) *J Phys Chem A* 118:1697. <https://doi.org/10.1021/jp4115699>
36. Weinhold F, Landis CR (2005) *Valency and bonding: a natural bond orbital donor-acceptor perspective*. Cambridge University Press, Cambridge
37. Ben Issa T, Sagaama A, Issaoui N (2020) *Comput Biol Chem* 86:107268. <https://doi.org/10.1016/j.compbiolchem.2020.107268>
38. Bader RFW (1990) *Atoms in molecules, a quantum theory*. Clarendon Press, Oxford
39. Rozas I, Alkorta I, Elguero J (2000) *J Am Chem Soc* 122:11154. <https://doi.org/10.1021/ja0017864>
40. Koch U, Popelier P (1995) *J Phys Chem* 99:9747. <https://doi.org/10.1021/j100024a016>
41. Saleh G, Gatti C, Lo Presti L, Contreras-Garcia J (2012) *Chemistry* 18:15523. <https://doi.org/10.1002/chem.201201290>
42. Lande DL, Bhadane SA, Gejji SP (2017) *J Phys Chem A* 121:1814. <https://doi.org/10.1021/acs.jpca.6b12912>
43. Johnson ER, Keinan S, Mori-Sanchez P, Contreras-García J, Cohen AJ, Yang W (2010) *J Am Chem Soc* 132:6498. <https://doi.org/10.1021/ja100936w>
44. Jomaa I, Noureddine O, Gatfaoui S, Issaoui N, Roisnel T, Marouani H (2020) *J Mol Struct* 1213:128186. <https://doi.org/10.1016/j.molstruc.2020.128186>
45. Issaoui N, Ghalla H, Muthu S, Flakus HT, Oujia B (2015) *Spectrochim Acta Part A Mol Biomol Spectrosc* 136:1227. <https://doi.org/10.1016/j.saa.2014.10.008>
46. Lewis DFV, Ioannides C, Parke DV (1994) *Xenobiotica* 24:401. <https://doi.org/10.3109/00498259409043243>
47. Issaoui N, Ghalla H, Brandán SA, Bardak F, Flakus HT, Atac A, Oujia B (2017) *J Mol Struct* 1135:209. <https://doi.org/10.1016/j.molstruc.2017.01.074>
48. Parr RG, Donnelly RA, Levy M, Palke WE (1977) *J Chem Phys* 68:3801. <https://doi.org/10.1063/1.436185>
49. Parr RG, Pearson RG (1983) *J Am Chem Soc* 105:7512. <https://doi.org/10.1021/ja00364a005>
50. Geerlings P, De Proft F, Langenaeker W (2003) *Chem Rev* 103:1793. <https://doi.org/10.1021/cr990029p>
51. Elleuch N, Amamou W, Ahmed AB, Abid Y, Feki H (2014) *Spectrochim Acta Part A Mol Biomol Spectrosc* 128:781. <https://doi.org/10.1016/j.saa.2014.02.159>
52. BevanOtt J, Boerio-Goates J (2000) *Chemical thermodynamics: principles and applications*. Academic Press, San Diego
53. Zhang R, Du B, Sun G, Sun Y (2010) *Spectrochim Acta Part A Mol Biomol Spectrosc* 75:1115. <https://doi.org/10.1016/j.saa.2009.12.067>
54. Çakmak Ş, Kansız S, Azam M, Ersanlı CC, İdil Ö, Veyisoğlu A, Yakan H, Küçük H, Chutia A (2022) *ACS Omega* 7(13):11320. <https://doi.org/10.1021/acsomega.2c00318>
55. Çakmak Ş, Kansız S, Azam M, Veyisoglu A, Yakan H, Min K (2022) *ACS Omega* 7:17192. <https://doi.org/10.1021/acsomega.2c00879>
56. Nakamoto K (1986) *Infrared and raman spectra of inorganic and coordination compounds part A; theory and applications in inorganic chemistry*. Wiley, New York, p 202
57. Durgun M, Ceylan Ü, Yalçın ŞP, Türkmen H, Özdemir N, Koyuncu İ (2016) *J Mol Struct* 114:95. <https://doi.org/10.1016/j.molstruc.2016.02.062>
58. Sert Y, Karakaya M, Çırak Ç, Eskiuyurt B, Kürekcı M (2015) *J Sulfur Chem* 36:450. <https://doi.org/10.1080/17415993.2015.1050397>
59. Fasano M, Curry S, Terreno E, Galliano M, Fanali G, Narciso P, Notari S, Ascenzi P (2005) *IUBMB Life*. 57:787. <https://doi.org/10.1080/15216540500404093>
60. Kragh-Hansen U (1985) *Biochem J* 225:629. <https://doi.org/10.1042/bj2250629>
61. Badraoui R, Saoudi M, Hamadou WS, Elkahoui S, Siddiqui AJ, Alam MJ, Suleiman AME, Alreshidi MM, Yadav DK, Nâïli H, Ben-Nasr H (2022) *Pharmaceuticals* 15:129. <https://doi.org/10.3390/ph15020129>
62. Badraoui R, Adnan M, Bardakci F, Alreshidi MM (2021) *Molecules* 26:673. <https://doi.org/10.3390/molecules26030673>
63. Ben-Nasr H, Badraoui R (2022) *Braz J Pharm Sci*
64. Badraoui R, Alrashedi MM, El-May MV, Bardakci F (2021) *J Biomol Struct Dynam* 39:6842. <https://doi.org/10.1080/07391102.2020.1803139>

Springer Nature or its licensor (e.g. a society or other partner) holds exclusive rights to this article under a publishing agreement with the author(s) or other rightsholder(s); author self-archiving of the accepted manuscript version of this article is solely governed by the terms of such publishing agreement and applicable law.